Multichannel spectrum of neutral particles trapped by a wire

James P. Burke, Jr., Chris H. Greene, and B. D. Esry
JILA and the Department of Physics, University of Colorado, Boulder, Colorado 80309-0440
(Received 6 May 1996)

The energy spectrum of a neutral atom bound in the magnetic field created by a straight line direct current is given by the Rydberg formula for particles with spin less than $\frac{3}{2}$. An adiabatic representation leads to a natural understanding of this spectrum and provides a good approximation to the bound state energy levels. A more accurate finite element method is applied to directly solve the time-independent Schrödinger equation for neutral particles with arbitrary spin. A combination of the finite element method with multichannel quantum defect theory provides a more efficient method to calculate the bound state energies. In addition, new spectral features arise for particles with spin greater than 1. [S1050-2947(96)00110-2]

PACS number(s): 32.80.Pj

I. INTRODUCTION

Schmiedmayer recently demonstrated that cold neutral atoms can be trapped and guided along a straight wire carrying a constant current [1]. The atomic magnetic moment interacts with the static magnetic field created by the current, trapping the atoms in Kepler-like orbits around the wire. This technique has the advantage of trapping the atoms in their *high-field-seeking state* [1,2]. The *high-field seeking state* is the ground state of the particle-field system and therefore does not suffer from spin exchange [3], which is a common loss mechanism in other types of neutral atom traps.

Pron'ko and Stroganov [4] proposed this type of magnetic trap some 20 years ago, and several authors [5–7] have investigated it theoretically since. Surprisingly, the energy spectrum for a spin-$\frac{1}{2}$ particle (and for the lowest angular momentum state of a spin-1 particle) obeys an exact hydrogenic Rydberg formula [4–7]. The proof of these analytical results assumes an infinitely thin wire; numerical calculations for wires of finite size [5] show that the bound states remain and that the energy spectrum still obeys a Rydberg formula with the inclusion of a quantum defect. Since the finite size of the wire does not qualitatively alter the spectrum, we treat only infinitely thin wires in this work.

The paper is organized in the following manner. We first derive the coupled time-independent radial Schrödinger equations for a neutral particle of arbitrary spin. A radially adiabatic representation is then developed that provides a simple, approximate solution whose quantitative accuracy suffices for many applications. The long-range interaction potential in this representation is proportional to ρ^{-1}, which leads to an infinite Rydberg energy spectrum (when the coefficient is negative). Section III bypasses the adiabatic representation and solves the coupled radial Schrödinger equations numerically for particles with spin $\frac{1}{2}$, 1, and $\frac{3}{2}$, using the finite element method [8,9]. One disadvantage of the direct approach is that the method can become memory intensive if very high energy levels are desired. A means of overcoming this problem while retaining the strengths of the finite element method is presented in Sec. IV, which adopts multichannel quantum defect theory (MQDT) techniques and divides configuration space into two regions. Finite elements are used to calculate an R matrix for the inner region, while the adiabatic representation is used to describe the outer region. Matching conditions at the region boundary then determine the bound state energies. In Sec. V, we investigate new multichannel phenomena that arise in the energy spectrum of a spin-$\frac{3}{2}$ particle. A spin-$\frac{3}{2}$ particle has two possible projections of the magnetic moment with a component parallel to the local magnetic field. Thus, two channels are capable of supporting bound states. Using a two-channel QDT model we show how channel coupling leads to perturbations of the energy level pattern. The feasibility of experimentally measuring the multichannel spectrum is also investigated.

II. ADIABATIC REPRESENTATION

A straight wire with constant current I flowing in the $\hat{z}$ direction produces an azimuthal magnetic field. A neutral spin particle in the presence of this field will experience an interaction that is given by

$$U_{\rm int} = -\vec{\mu}\cdot\vec{B} = -\left(\frac{g\mu_B}{\hbar}\right)\vec{S}\cdot\vec{B}, \tag{1}$$

where $\vec{B} = (\mu_0 I/2\pi\rho)\hat{\phi}$ in SI units, g is the gyromagnetic ratio, and μ_B the Bohr magneton. The interaction potential is independent of z. Therefore, the motion of the particle along the wire is free, and the z dependence of the Hamiltonian can be separated out, leaving only the transverse motion as a nontrivial problem. We focus only on the transverse motion here. The potential can be rewritten in terms of the spin raising and lowering operators. In the representation where S_z is diagonal, the interaction potential is given by the following expression

$$U_{\rm int} = -\frac{iG}{\rho}(e^{i\phi}S_- - e^{-i\phi}S_+), \tag{2}$$

where the constant $G = g\mu_B\mu_0 I/4\pi$. The final form of the two-dimensional Schrödinger equation becomes

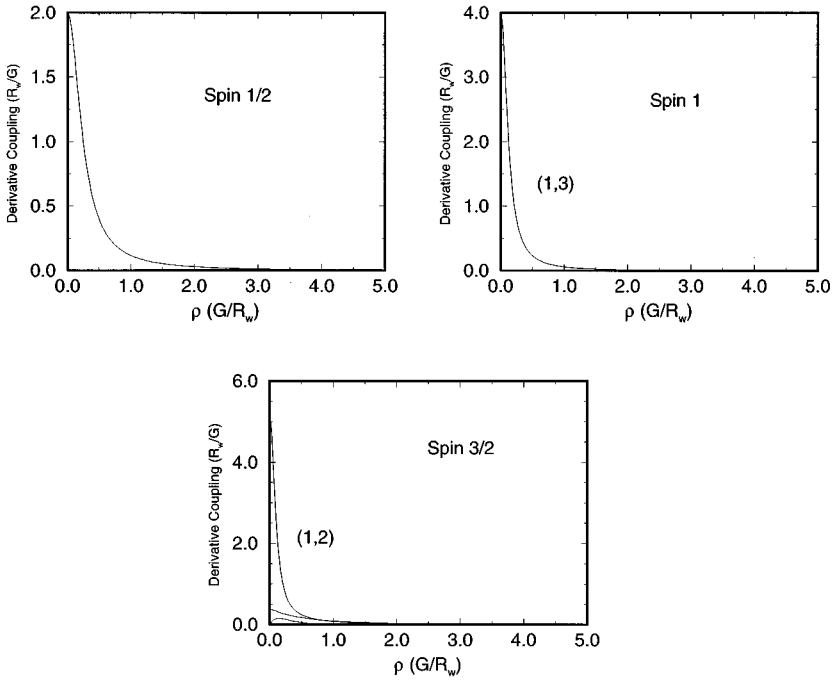

FIG. 1. Derivative coupling matrix elements for the lowest angular momentum state ν_z of a spin-$\frac{1}{2}$, -1, and -$\frac{3}{2}$ particle given in units of $R_w/G=MG/\hbar^2$. Coupling between the lowest channel and all other channels shown. The radius is given in units of $G/R_w=\hbar^2/MG$.

$$\left[-\frac{\hbar^2}{2M}\nabla^2_{\rho,\phi}-\frac{iG}{\rho}(e^{i\phi}S_- - e^{-i\phi}S_+)\right]\Psi(\rho,\phi,\sigma) = E\Psi(\rho,\phi,\sigma), \tag{3}$$

where $\nabla^2_{\rho,\phi}=\partial^2/\partial\rho^2+(1/\rho)\partial/\partial\rho+(1/\rho^2)\partial^2/\partial\phi^2$ and where σ denotes the spin degrees of freedom. The operator $J_z=L_z+S_z$ commutes with the Hamiltonian and the eigenvalues ν_z of J_z are constants of the motion. Following the derivation of Blümel and Dietrich, we expand the ϕ dependence and σ dependence in a complete orthonormal set. For a given ν_z, this expansion reads

$$\Psi(\rho,\phi,\sigma)=\sum_m \Omega_m(\phi,\sigma)F_m(\rho), \tag{4}$$

where $\Omega_m=i^{S-m}e^{i(\nu_z-m)\phi}\sigma_m$, S is the total spin of the particle, and the summation is over the eigenvalues m of S_z. Inserting this expansion into Eq. (3) leads to a set of $(2S+1)$ coupled radial equations. In the next section these coupled equations are solved directly with a finite element radial basis set, but it is first instructive to develop a radially adiabatic representation. We develop it for a spin-$\frac{1}{2}$ particle, but the equations are readily generalized to particles with higher spin.

The coupled equations for a spin-$\frac{1}{2}$ particle are

$$\left[-\frac{\hbar^2}{2M}\left(\frac{d^2}{d\rho^2}+\frac{1}{\rho}\frac{d}{d\rho}\right)+\frac{\hbar^2(\nu_z-1/2)^2}{2M\rho^2}\right]F_+ - \frac{G}{\rho}F_- = EF_+,$$

$$\left[-\frac{\hbar^2}{2M}\left(\frac{d^2}{d\rho^2}+\frac{1}{\rho}\frac{d}{d\rho}\right)+\frac{\hbar^2(\nu_z+1/2)^2}{2M\rho^2}\right]F_- - \frac{G}{\rho}F_+ = EF_-. \tag{5}$$

Choosing ρ as the adiabatic coordinate, the Hamiltonian can be separated into two terms $H=T_\rho+H^{\rm ad}$, where the kinetic energy operator T_ρ contains all the derivative terms with respect to ρ. The adiabatic Hamiltonian $H^{\rm ad}$ is given in matrix notation by

$$H^{\rm ad}=\begin{pmatrix} \dfrac{\hbar^2(\nu_z-1/2)^2}{2M\rho^2} & -\dfrac{G}{\rho} \\ -\dfrac{G}{\rho} & \dfrac{\hbar^2(\nu_z+1/2)^2}{2M\rho^2}\end{pmatrix}. \tag{6}$$

Adiabatic eigenfunctions χ_γ and eigenvalues (adiabatic potentials) U_γ of $H^{\rm ad}$ are calculated at each value of ρ. The wave function can then be written in terms of the adiabatic eigenfunctions [13,14]

$$\Psi=\sum_\gamma \Phi_\gamma(\phi,\sigma;\rho)M_\gamma(\rho), \tag{7}$$

where $M_\gamma(\rho)=\Sigma_{m'}\chi^\top_{\gamma m'}F_{m'}$ and $\Phi_\gamma(\phi,\sigma;\rho)=\Sigma_m\Omega_m\chi_{m\gamma}$. Substituting this expansion back into the Hamiltonian gives the following representation for the coupled radial equations:

$$\left[\left(\underline{I}\frac{d}{d\rho}+\underline{P}\right)^2+\frac{1}{\rho}\left(\underline{I}\frac{d}{d\rho}+\underline{P}\right)+\frac{2M}{\hbar^2}(\underline{I}E-\underline{U})\right]\vec{M}=0. \tag{8}$$

All of the coupling (or nonadiabatic) effects are now contained in the derivative coupling matrix $\underline{P}(\rho)$ given by

$$P_{\gamma\gamma'}=\left\langle \Phi_\gamma\left|\frac{d}{d\rho}\Phi_{\gamma'}\right.\right\rangle. \tag{9}$$

The Born-Oppenheimer approximation amounts to total neglect of the $\underline{P}$ matrix. In the limit $\underline{P}\to 0$, the adiabatic approximation becomes an exact formulation. Some methods treat the full vector adiabatically, in contrast to the present scheme which treats only ρ adiabatically. Examples of the $\underline{P}$ matrix elements are shown in Fig. 1 for the lowest angular momentum states of a particle with spin $\frac{1}{2}$, 1, or $\frac{3}{2}$. The graphs show that channel coupling primarily affects the short-range physics and becomes negligible as ρ becomes

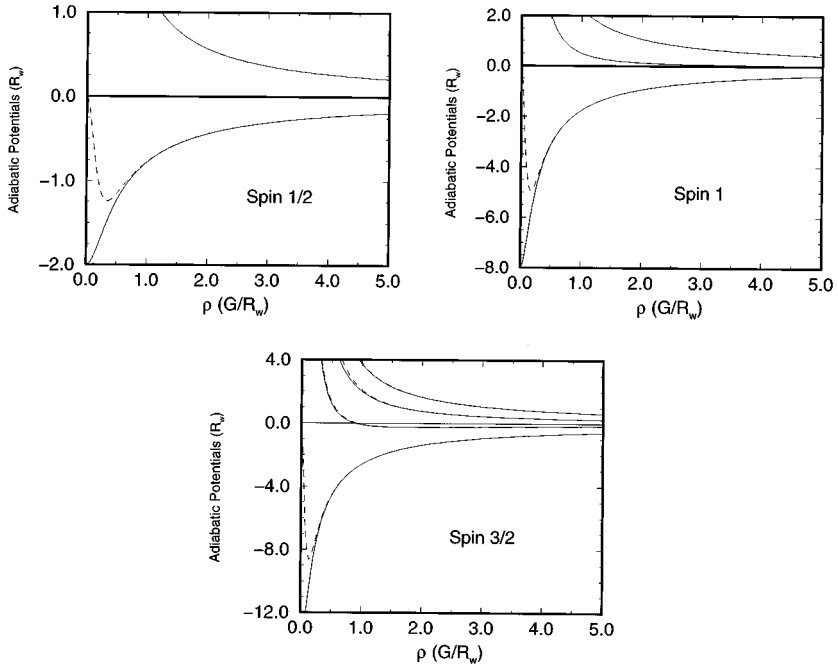

FIG. 2. Adiabatic potentials for the lowest angular momentum state of a spin-$\frac{1}{2}$, -1, and -$\frac{3}{2}$ particle. Dashed lines indicate the potentials with diagonal corrections. Energies are in units of $R_w = MG^2/\hbar^2$ and the radius is given in units of $G/R_w = \hbar^2/MG$.

large. The adiabatic approximation thus provides a good description of the long-range physics; consequently the motion of a trapped particle can be described by the equivalent motion of a particle bound in a one-dimensional adiabatic potential curve. Adiabatic potentials for the lowest angular momentum states are shown in Fig. 2. Focusing on the attractive potentials, it can be seen that the asymptotic behavior is $U_\gamma(\rho) \rightarrow -c_\gamma \rho^{-1}$, where the constant c_γ depends on both the spin quantum number S and the channel index γ. The motion of a particle in an adiabatic potential is analogous to electron motion in a modified Coulomb potential, for which the energy spectrum is given by a Rydberg formula with a nonzero quantum defect μ [11,12]. The adiabatic approximation improves for higher angular momentum states owing to the stronger centrifugal barrier. The short-range coupling effects occur predominantly in the classically forbidden region ''underneath'' the centrifugal barrier, whereby the nonadiabatic effects are largely ''hidden'' from the particle. This can be seen in Fig. 3, which shows the adiabatic potentials and derivative coupling element $P_{12}(\rho)$ for a spin-$\frac{1}{2}$ particle with $\nu_z = \frac{11}{2}$.

We can gain further physical insight into the adiabatic approximation by examining the ρ dependence of the S_ϕ operator in the adiabatic representation. Figure 4 shows that the expectation values of S_ϕ for the adiabatic eigenstates converge to $\pm\frac{1}{2}$ as ρ increases. The adiabatic basis therefore describes spin eigenstates that are aligned either parallel or antiparallel with the magnetic field at large ρ. In this regime, the adiabatic frame is equivalent to a frame rotating with the particle. However, the expectation values of S_ϕ decrease dramatically as ρ becomes small. The breakdown of the adiabatic approximation at small ρ is the result of neglecting the radial kinetic energy operator. In a classical sense, a particle in an ellipitical orbit with a minimum radius very near the wire experiences a sudden change in its radial kinetic energy as it ''whips'' around the wire. This nonadiabatic effect is manifested in the $\underline{P}$ matrix elements. The $\underline{P}$ matrix elements are therefore in a sense describing the ability of the adiabatic basis to represent spin eigenstates that stay aligned parallel or antiparallel with the magnetic field.

The effectiveness of this adiabatic representation can be gauged through the accuracy of the bound state energies predicted by the adiabatic approximation. For low angular momentum states, it is necessary to include some of the diagonal short-range nonadiabatic corrections. We have done this in the manner of Klar and Fano [13,14] by adding diagonal corrections to the Born-Oppenheimer type potentials,

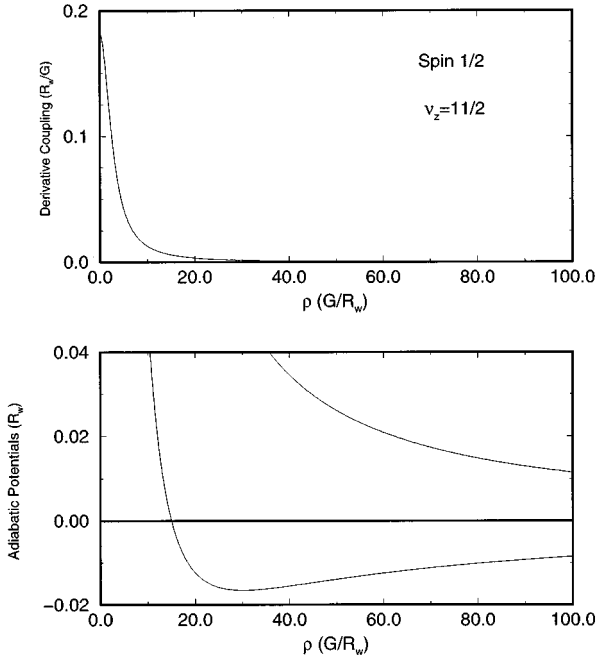

FIG. 3. Adiabatic potentials and derivative coupling matrix element for a spin-$\frac{1}{2}$ particle with $\nu_z = \frac{11}{2}$. The potentials with diagonal corrections are also plotted but cannot be distinguished on this scale. Energies are in units of $R_w = MG^2/\hbar^2$ and the radius is given in units of $G/R_w = \hbar^2/MG$.

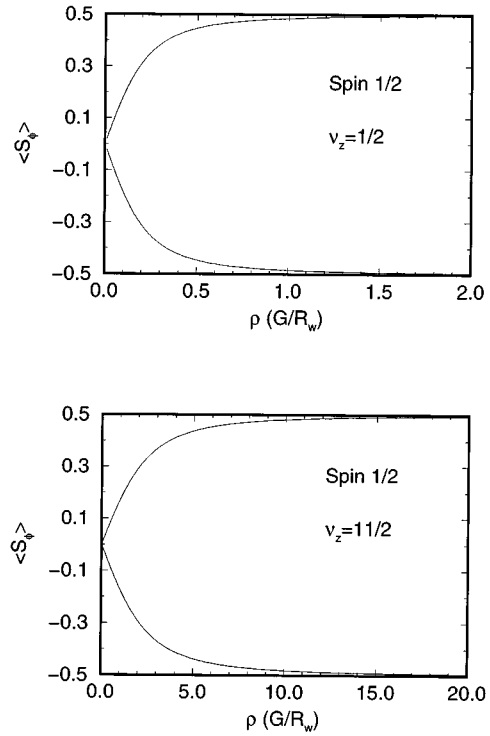

FIG. 4. Expectation values of the $S_{\hat{\phi}}$ operator in the adiabatic representation (in units of $\hbar$). Radius is given in units of $G/R_w=\hbar^2/MG$.

$U_\gamma^c=U_\gamma-(\hbar^2/2M)(\underline{P}^2)_{\gamma\gamma}$. The corrected potentials are also shown in Fig. 2. In Table I, adiabatic energy level predictions obtained with the corrected potentials are compared to the analytical results for a spin-$\frac{1}{2}$ particle. The energy levels are given by

$$E_{n,\nu_z}=-\frac{R_w}{2(n+|\nu_z|-\mu-\frac{1}{2})^2}, \tag{10}$$

with $n\geqslant 1$ and reduce to the analytical result [4–6] when the quantum defect $\mu=0$. R_w is defined to be a characteristic unit of energy given by $R_w=MG^2/\hbar^2$. The adiabatic predictions differ in quantum defect from the exact results by approximately $\Delta\mu=-0.016$. The adiabatic approximation improves dramatically for higher angular momentum states, as evidenced by the tabulated energies for the $\nu_z=\frac{11}{2}$ state (see Table II), which are very close to the exact energies (both with and without diagonal corrections). The adiabatic representation thus provides a good first-order approximation to the energy levels and a simple qualitative picture for the quantum mechanical motion of the neutral particle.

TABLE I. Comparison of exact energies ($E_n=-1/2n^2$) with energy levels calculated using an adiabatic potential with diagonal corrections, for a spin-$\frac{1}{2}$ particle with $\nu_z=\frac{1}{2}$. The discrepancy $\Delta\mu$ is the quantum defect associated with the adiabatic calculation. Energies are given in units of $R_w=MG^2/\hbar^2$. Numbers in brackets denote powers of 10.

n	Exact	Adiabatic	$\Delta\mu$
1	−0.50000	−0.48923	−1.09 [−2]
2	−0.12500	−0.12320	−1.46 [−2]
3	−0.05556	−0.05499	−1.53 [−2]
4	−0.03125	−0.03101	−1.56 [−2]
5	−0.02000	−0.01987	−1.57 [−2]
6	−0.01389	−0.01382	−1.58 [−2]
7	−0.01020	−0.01016	−1.58 [−2]
8	−0.00781	−0.00778	−1.58 [−2]
9	−0.00617	−0.00615	−1.59 [−2]
10	−0.00500	−0.00498	−1.59 [−2]

III. FINITE ELEMENT METHOD

We now turn to a more accurate quantitative description of the spectrum. The $(2S+1)$ coupled radial equations are solved numerically using a finite element method. The finite element method truncates the domain of the radial variable ρ to $0\leqslant\rho\leqslant\rho_c$ and divides the truncated domain into sectors (or elements). The cutoff radius ρ_c is chosen large enough to permit neglect of the wave function at larger distances, and the boundary condition $F(\rho_c)=0$ is imposed. For the present problem, we have chosen the sector boundaries to conform to a square root grid $\rho_i\propto i^2$, which produces a roughly constant number of sectors per oscillation of the wave function.

The radial wave function $F_m(\rho)$ in channel m is written as a sum over the sectors i of functions defined only in that sector

$$F_m(\rho)=\sum_i f_{im}(x_i). \tag{11}$$

Here, x_i is defined over the interval $[-1,1]$, which is mapped to the physical sector $[\rho_i,\rho_{i+1}]$ using the transformation

$$\rho=a_i x_i+t_i,$$

$$a_i=\frac{\rho_{i+1}-\rho_i}{2},$$

$$t_i=\frac{\rho_{i+1}+\rho_i}{2}. \tag{12}$$

The function f_{im} is then expanded in terms of a local basis as

$$f_{im}(x_i)=\sum_{k=1}^{6} c_k^{im}u_k(x_i). \tag{13}$$

The local basis functions u_k are fifth-order Hermite interpolating polynomials, which satisfy the following conditions:

$$u_k(-1)=\delta_{1k},\quad u_k(0)=\delta_{3k},\quad u_k(1)=\delta_{5k},$$

$$u_k'(-1)=\delta_{2k},\quad u_k'(0)=\delta_{4k},\quad u_k'(1)=\delta_{6k}. \tag{14}$$

Note that $u_k(x_i)$ is nonzero only in the ith sector and the $u_k(x_i)$ functions are nonorthogonal in that sector. We further require the wave function and its first derivative to be continuous across each sector boundary, which imposes the following constraints on the coefficients of the local basis functions [15]:

TABLE II. Comparison of exact energies with energy levels calculated using adiabatic potentials [with and without diagonal corrections (DC)] for a spin-$\frac{1}{2}$ particle with $\nu_z=\frac{11}{2}$. The discrepancy $\Delta\mu$ is the quantum defect determined by the adiabatic calculations. Energies are given in units of $R_w=MG^2/\hbar^2$. Numbers in brackets denote powers of 10.

n	Exact	Adiabatic (DC)	$\Delta\mu$	Adiabatic (no DC)	$\Delta\mu$
1	−0.01388889	−0.01388879	−2.2 [−5]	−0.01388976	1.88 [−4]
2	−0.01020408	−0.01020396	−4.3 [−5]	−0.01020463	1.87 [−4]
3	−0.00781250	−0.00781239	−5.7 [−5]	−0.00781286	1.87 [−4]
4	−0.00617284	−0.00617275	−6.6 [−5]	−0.00617310	1.86 [−4]
5	−0.00500000	−0.00499993	−7.2 [−5]	−0.00500019	1.86 [−4]
6	−0.00413223	−0.00413217	−7.7 [−5]	−0.00413237	1.86 [−4]
7	−0.00347222	−0.00347218	−8.1 [−5]	−0.00347233	1.86 [−4]
8	−0.00295858	−0.00295854	−8.4 [−5]	−0.00295866	1.85 [−4]
9	−0.00255102	−0.00255099	−8.6 [−5]	−0.00255109	1.85 [−4]
10	−0.00222222	−0.00222220	−8.8 [−5]	−0.00222228	1.85 [−4]

$$c_5^{im}=c_1^{i+1,m},\quad c_6^{im}=\frac{a_i}{a_{i+1}}c_2^{i+1,m}. \tag{15}$$

We can now define local Hamiltonian and overlap block matrices $\underline{H}^i$ and $\underline{S}^i$ for each sector i. For an N_c channel problem, the local matrices are divided into N_c^2 blocks. The diagonal blocks contain channel specific contributions and off-diagonal blocks contain any channel coupling contributions. The matrix elements are given by

$$H_{kl}^{imm'}=\int_{-1}^{1}u_k^{im'}Hu_l^{im}a_i(a_ix_i+t_i)dx_i \tag{16}$$

and

$$S_{kl}^{imm'}=\delta_{m,m'}\int_{-1}^{1}u_k^{im'}u_l^{im}a_i(a_ix_i+t_i)dx_i. \tag{17}$$

The notation $H_{kl}^{imm'}$ refers to the matrix element in row k, column l of block mm'. The local matrices are combined [9] including the sector boundary conditions [Eq. (15)] to form the global matrices $\underline{H}$ and $\underline{S}$, which are banded, symmetric, and sparse. The Schrödinger equation (5) is transformed into the generalized eigenvalue equation

$$\underline{H}\vec{c}=E\underline{S}\vec{c}. \tag{18}$$

TABLE III. Comparison of exact energies with energy levels obtained from a numerical finite element calculation for a spin-$\frac{1}{2}$ particle with $\nu_z=\frac{1}{2}$. The discrepancy $\Delta\mu$ is the quantum defect associated with the finite element calculation. Energies are given in units of $R_w=MG^2/\hbar^2$. Numbers in brackets denote powers of 10.

n	Exact	Finite elements	$\Delta\mu$
1	−0.5000000000	−0.4999999699	−3.0 [−8]
2	−0.1250000000	−0.1249999963	−3.0 [−8]
3	−0.0555555556	−0.0555555544	−3.0 [−8]
4	−0.0312500000	−0.0312499995	−3.0 [−8]
5	−0.0200000000	−0.0199999997	−3.1 [−8]

The dimension of the system is equal to $N_c(4N_s+1)$, where N_c is the number of channels and N_s is the number of sectors. Standard EISPACK routines [16] were used to solve Eq. (18).

Finite element results for the lowest total angular momentum state for a spin-$\frac{1}{2}$ particle are compared to the exact results in Table III. These results were obtained with a cutoff radius $\rho_c=130$ in units of $\hbar^2/MG$ and a 31 sector mesh [roughly 4 sectors between consecutive wave-function nodes; 10 sectors were added between $0.0\leqslant\rho\leqslant0.6$ to handle the $\ln(\rho)$ indicial behavior of one component of the total wave function]. Finite element method (FEM) results for the lowest angular momentum states of a spin-1 and a spin-$\frac{3}{2}$ particle are presented in Table IV. These results were obtained with the same cutoff radius and sector grid. In addition, we present a comparison (see Table V) between our FEM results for higher angular momentum states of a spin-1 particle with previous numerical calculations presented in Ref. [7]. Good agreement between the two different calculations is seen except for the $\nu_z=1$ angular momentum case.

IV. COMBINED FEM-MQDT TREATMENT

If very high Rydberg states are needed, the direct solution of Eq. (18) can become quite memory intensive. Multichannel quantum defect theory provides a method for obtaining these states while retaining the accuracy of the finite element

TABLE IV. Finite element bound state energy results for a spin-1 particle with $\nu_z=0$ and a spin-$\frac{3}{2}$ particle with $\nu_z=\frac{1}{2}$. The discrepancy $\Delta\mu$ is the quantum defect associated with the FEM calculation for the spin-1 case. The exact solution for this case is provided in Ref. [7]. Energies are given in units of $R_w=MG^2/\hbar^2$. Numbers in brackets denote powers of 10.

n	Spin 1	$\Delta\mu$	Spin 3/2
1	−1.99999950	−1.25 [−7]	−3.67346791
2	−0.49999993	−1.42 [−7]	−1.00461454
3	−0.22222220	−1.51 [−7]	−0.46255162
4	−0.12499999	−1.59 [−7]	−0.26509196
5	−0.07999999	−1.66 [−7]	−0.17162858

TABLE V. Comparison of the FEM bound state energies with energy solutions published in Ref. [7] (which will be referred to as BSBGH) for a spin-1 particle. Energies are given in units of $2R_w=2MG^2/\hbar^2$ and $N=n+|\nu_z|-1$.

	$\nu_z=1$		$\nu_z=2$		$\nu_z=3$		$\nu_z=4$	
N	FEM	BSBGH	FEM	BSBGH	FEM	BSBGH	FEM	BSBGH
4	−0.0543	−0.0527	−0.052080	−0.052079	−0.0512134	−0.0512134	−0.05076228	−0.05076227
3	−0.0922	−0.0891	−0.087435	−0.087435	−0.08555613	−0.08555612		
2	−0.1903	−0.1815	−0.1762889	−0.1762887				
1	−0.600	−0.555						

method. The MQDT approach divides configuration space into two regions. The division is chosen such that the channel coupling can be neglected in the outer region, which makes the solutions simpler there. For our purposes, this is accomplished by choosing a radius ρ_0 such that the derivative coupling matrix $\underline{P}(\rho)$ is negligible for $\rho>\rho_0$. A finite element R-matrix approach is used for the inner region solution, while the adiabatic approximation is used in the outer region. A determinantal matching condition, involving the inner and outer solutions at the boundary, determines whether a physically valid solution exists at any particular energy E.

The variational R-matrix method [17] requires the solution of the following generalized eigenvalue equation at a given energy E:

$$\underline{\Gamma}\,\vec{c}=b\underline{\Lambda}\,\vec{c}, \tag{19}$$

where b is the eigenchannel logarithmic derivative. The $\underline{\Gamma}$ matrix in the finite element representation is given locally by

$$\Gamma_{kl}^{imm'}=\frac{2M}{\hbar^2}\int_{-1}^{1}u_k^{im'}(E-H)u_l^{im}a_i(a_ix_i+t_i)dx_i$$

$$-\frac{\rho_0}{a_i}\delta_{i,N_s}\delta_{m,m'}\delta_{k5}\delta_{l6}. \tag{20}$$

The integrals are independent of E and only need to be evaluated once. The local matrices are combined together to form a single global matrix $\underline{\Gamma}$. The $\underline{\Lambda}$ matrix elements are surface integrals, which in the finite element representation are nonzero only in the last sector so that

$$\Lambda_{kl}^{N_s mm'}=\rho_0\delta_{m,m'}\delta_{k5}\delta_{l5}. \tag{21}$$

The matrices are again banded, symmetric, sparse, and small enough for the EISPACK routines to solve Eq. (19) efficiently.

The generalized eigensystem is solved using open boundary conditions such that the wave function is allowed to be nonzero at the outer boundary ρ_0. The R matrix is formed from the nontrivial eigenvalues and corresponding eigenvectors according to

$$R_{mm'}=\sum_{\beta}Z_{m\beta}b_{\beta}^{(s)}Z_{\beta m'}^{\top}, \tag{22}$$

where the logarithmic derivative $b_\beta^{(s)}$ has been rescaled to remove first-order radial derivative contributions to the kinetic energy operator. Here β distinguishes the linearly independent solutions. $Z_{m\beta}$ is given by the normalized projection of the mth channel wave function onto the βth solution at the boundary ρ_0. This is the inverse of the ''usual'' R-matrix definition given in Ref. [17]. In the finite element representation, the projection is simply given by the coefficient $c_{5\beta}^{N_s m}$ of the u_5 basis function in the last sector for each channel and each independent solution

$$Z_{m\beta}=\frac{c_{5\beta}^{N_s m}}{N_\beta}, \tag{23}$$

where $N_\beta=\sqrt{\Sigma_m(c_{5\beta}^{N_s m})^2}$. The R matrix is then transformed using the adiabatic eigenvectors

$$\underline{R}^{\mathrm{ad}}=\underline{\chi}^{\top}(\rho_0)\underline{R}(\rho_0)\underline{\chi}(\rho_0). \tag{24}$$

A bound state at energy E occurs if a linear combination of the independent solutions can be found that matches, at the boundary ρ_0, a wave function that asymptotically behaves as a decaying exponential. This condition can be stated as

$$-\frac{\Sigma_\beta Z_{\gamma\beta}^{\mathrm{ad}}d_\beta}{\Sigma_\beta Z_{\gamma\beta}^{\mathrm{ad}}b_\beta d_\beta}=\frac{W_\gamma(\rho_0)}{W_\gamma'(\rho_0)}, \tag{25}$$

where $Z_{\gamma\beta}^{\mathrm{ad}}=\Sigma_m\chi_{\gamma m}^{\top}Z_{m\beta}$, d_β are constant coefficients, and $W_\gamma(\rho_0)$ represents the value of the outer region wave function in the adiabatic channel γ at the boundary. The matching condition can be rewritten in the form of a determinantal equation

$$\det|\underline{R}^{\mathrm{ad}}+\underline{B}^{-1}|=0, \tag{26}$$

where $\underline{B}^{-1}$ is a diagonal matrix, each of whose diagonal elements is given by the inverse of the right-hand side of Eq. (25).

In the approximation used here, the outer region wave function $W_\gamma(\rho)$ obeys the Schrodinger equation

$$W_\gamma''(\rho)+\frac{2M}{\hbar^2}[E-U_\gamma(\rho)]W_\gamma(\rho)=0, \tag{27}$$

where $U_\gamma(\rho)$ is the adiabatic potential for channel γ. It is convenient to define a ''phase function'' ϕ such that

$$\phi_\gamma(\rho)=\cot^{-1}\left(\frac{W_\gamma'(\rho)}{W_\gamma(\rho)}\right), \tag{28}$$

because ϕ_γ obeys a simple first-order nonlinear differential equation [18]:

TABLE VI. Comparison of the combined R-matrix and FEM approach with a direct finite element calculation for the bound state energies of a spin-$\frac{3}{2}$ particle with $\nu_z=\frac{3}{2}$. A matching radius $\rho_0 = 20.0$ in units of $\hbar^2/MG$ was used. The quantum defects μ_1 are associated with channel 1 and are given modulo unity. Energies are given in units of $R_w=MG^2/\hbar^2$.

	Finite element		R matrix	
n	Energy	Quantum defect (μ_1)	Energy	Quantum defect (μ_1)
7	−0.08307431	−0.359917	−0.08307455	−0.359906
8	−0.07900489	0.452914	−0.07900460	0.452901
9	−0.06160194	0.453091	−0.06160159	0.453067
10	−0.04937224	0.453046	−0.04937166	0.452989
11	−0.04194325	−0.357984	−0.04194306	−0.358008
12	−0.04044738	0.452220	−0.04044884	0.452411
13	−0.03374812	0.452673	−0.03374814	0.452677
14	−0.02858350	0.452750	−0.02858329	0.452703
15	−0.02522217	−0.357188	−0.02522145	−0.357379

$$\phi'_\gamma(\rho)=\frac{2M}{\hbar^2}[E-U_\gamma(\rho)]\sin^2\phi_\gamma+\cos^2\phi_\gamma. \qquad (29)$$

The differential equation is integrated inward from a large distance with a standard fourth-order Runge-Kutta routine to obtain the matrix elements $\underline{B}^{-1}$ at ρ_0.

After $\underline{R}^{\rm ad}$ is inserted into Eq. (26), the bound state energies are found through a numerical search for roots of that equation. Table VI compares the results obtained by this method with direct finite element solutions for the energy levels of a spin-$\frac{3}{2}$ particle in the field of a linear current. The FEM solutions are converged to all digits shown in the table so we see a small loss in accuracy with the R-matrix matching method. However, this approach does provide a much more efficient use of computer resources as compared to the direct diagonalization of very large matrices and by increasing the boundary radius the accuracy of the solutions can be improved.

V. TWO-CHANNEL QDT ANALYSIS

A spin-$\frac{3}{2}$ particle possesses two channels that support bound states (Fig. 5). The channels are coupled and the energy levels in the two channels can therefore perturb each other. A two-channel quantum defect analysis can help to interpret these perturbations.

We start by dividing configuration space into two regions. The boundary radius ρ_0 is chosen, such that, at a given energy $E<0$ the two attractive channels are ''locally'' open; this means the effective radial kinetic energy $E-U_\gamma(\rho)$ is positive at ρ_0. The outer region solution matrix can be written, after exponential decay is enforced in the upper two adiabatic channels that possess no bound states, as

$$M_{\gamma\gamma'}(\rho)=f_\gamma(\rho)\,\delta_{\gamma\gamma'}-g_\gamma(\rho)K_{\gamma\gamma'}. \qquad (30)$$

Here the index γ denotes the channel component, while the index γ' distinguishes the different linearly independent solutions. The asymptotic solution matrix $\underline{M}(\rho)$ contains a set

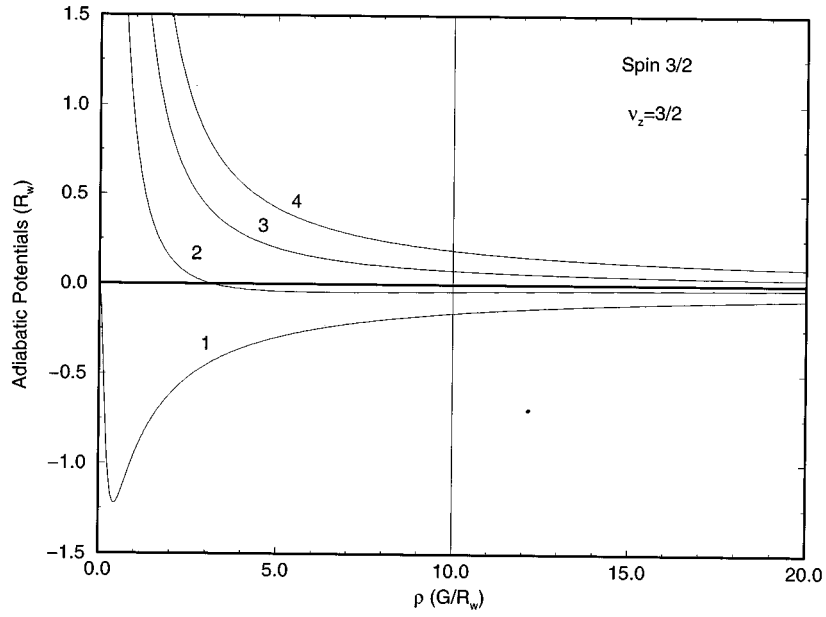

FIG. 5. Adiabatic potentials with diagonal corrections for a spin-$\frac{3}{2}$ particle with $\nu_z=\frac{3}{2}$. The boundary radius $\rho_0=10.0$ in units of $G/R_w=\hbar^2/MG$ is marked. Energy is given in units of $R_w=MG^2/\hbar^2$.

of linearly independent solutions of the Schrödinger equation that are determined by matching the inner region solution matrix and its radial derivative on the boundary ρ_0 to a linear combination of Coulomb functions (f,g) in the two lower channels. The $\underline{K}$ matrix is the usual short-range reaction matrix of multichannel quantum defect theory. It identifies the appropriate linear combination of regular, f_γ, and irregular, g_γ, radial Coulomb functions, which matches the outer wave function smoothly to the numerically determined inner-region solution. This $\underline{K}$ matrix controls the asymptotic form of the solution as in standard multichannel quantum defect treatments [10,11]. The leading term of the asymptotic form of the Coulomb functions (in the channels that experience an attractive ρ^{-1} behavior at $\rho\to\infty$ only, and at $E<0$ [10]) is given by

$$f_\gamma \to e^{\kappa\rho}\sin\pi(\nu_\gamma-\lambda_\gamma) \tag{31}$$

and

$$g_\gamma \to -e^{\kappa\rho}\cos\pi(\nu_\gamma-\lambda_\gamma). \tag{32}$$

Here ν_γ is the effective quantum number in channel γ and λ_γ is a real noninteger, channel dependent constant that depends on the eigenvalue of J_z. The exact form of the dependence of λ_γ on J_z is not required in our final model if we adopt a rotated version of the Coulomb functions $\tilde{f}$ and $\tilde{g}$, defined by

$$\begin{pmatrix}\tilde{f}\\ \tilde{g}\end{pmatrix}=\begin{pmatrix}\cos\pi\lambda_\gamma & -\sin\pi\lambda_\gamma\\ \sin\pi\lambda_\gamma & \cos\pi\lambda_\gamma\end{pmatrix}\begin{pmatrix}f_\gamma\\ g_\gamma\end{pmatrix}. \tag{33}$$

The outer region solution matrix can then be rewritten as

$$\underline{M}=\underline{\tilde{f}}-\underline{\tilde{g}}\,\underline{\tilde{K}}, \tag{34}$$

where $\underline{\tilde{f}}$ and $\underline{\tilde{g}}$ are diagonal matrices. At this point, physically valid solutions can be obtained by imposing the large-ρ boundary conditions. This is accomplished in two steps.

The boundary conditions at $E<0$ require the channel wave functions to decay exponentially at $\rho\to\infty$. This decay is obtained through a transformation that forms a linear combination of independent solutions for which the exponentially growing term in each channel disappears [10,12]. The most convenient procedure for our present needs is to eliminate the exponential growth initially in the upper attractive channel (i.e., channel 2 in Fig. 5). This leads to an energy-dependent single channel quantum defect in the remaining attractive channel:

$$\tan\pi\tau(E)=\tilde{K}_{11}-\tilde{K}_{12}[\tan\pi\nu_2+\tilde{K}_{22}]^{-1}\tilde{K}_{21}. \tag{35}$$

Application of the final large ρ boundary condition in channel 1 requires τ to satisfy the bound state quantization condition

$$\tau=n-\nu_1. \tag{36}$$

Exact calculations of the $\underline{\tilde{K}}$ matrix are somewhat complicated numerically, in general. Rather than perform the complete *ab initio* calculation this way, we have analyzed the spectrum using this procedure by fitting the $\underline{\tilde{K}}$ matrix to the accurate levels calculated in the preceding section. In this formulation, the ''strength'' of the channel interactions is governed by the coupling parameters $\tilde{K}_{12},\tilde{K}_{11},\tilde{K}_{22}$ which have been assumed to be nearly energy independent over this small range of interest. Accurate energies obtained from the FEM were used as input data for the fit. These energies were used to find approximate linear expressions for the diagonal reaction matrix elements $\tilde{K}_{11}$and $\tilde{K}_{22}$ versus E. The coupling parameter $\tilde{K}_{12}$ was varied to determine the optimum fit to the FEM data. Figure 6 shows a Lu-Fano plot of the best fit for a particle in an angular momentum state $\nu_z=\frac{3}{2}$. In the limit $\tilde{K}_{12}\to 0$, the energy spectrum would consist of two overlapping but noninteracting Rydberg series given by

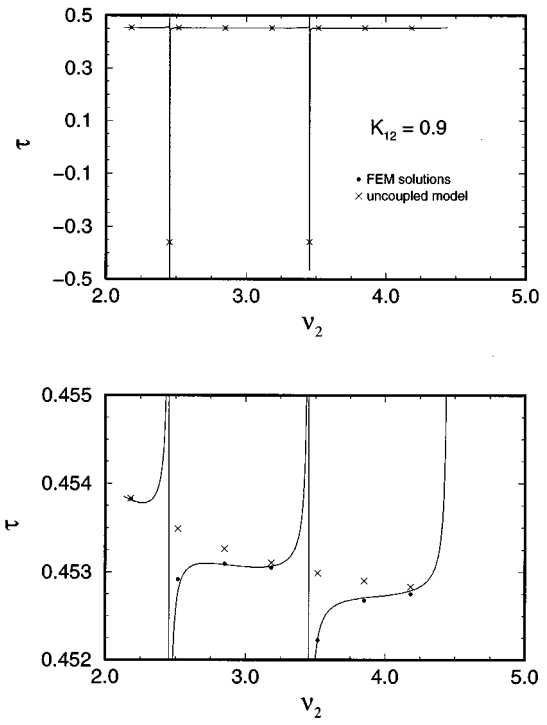

FIG. 6. The model $\underline{\tilde{K}}$ matrix parameter τ versus energy. The data points were obtained from the FEM energy results ($\nu_z=\frac{3}{2}$ state) referenced in Table VI. The uncoupled model energy data points were calculated using Eqs. (37) and (38). The parameter τ was calculated with the coupling coefficient $\tilde{K}_{12}=0.90$. ν_2 is the effective quantum number in channel 2. A blowup of the first plot is also shown.

$$E_1=-\frac{9MG^2}{2\hbar^2(n_1-\mu_1)^2} \tag{37}$$

and

$$E_2=-\frac{MG^2}{2\hbar^2(n_2-\mu_2)^2}, \tag{38}$$

where $\mu_1=\arctan(\tilde{K}_{11})/\pi$ and $\mu_2=\arctan(\tilde{K}_{22})/\pi$ are single channel quantum defects. The deviations in τ between the coupled and uncoupled models are seen to be the largest for the energies at which E_1 and E_2 nearly coincide. The chan-

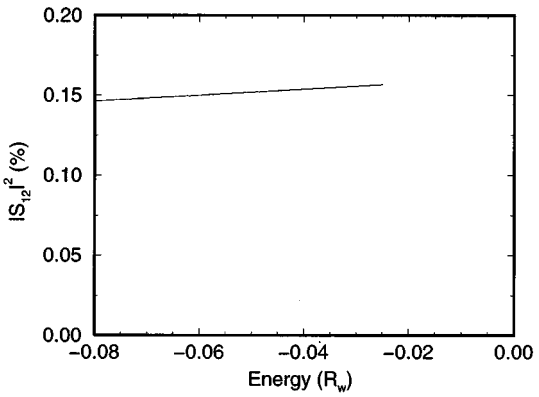

FIG. 7. The absolute value squared of the scattering matrix element S_{12} vs energy. The $\underline{S}$ matrix was calculated from the model $\underline{\widetilde{K}}$ matrix with the coupling coefficient $\widetilde{K}_{12}=0.90$. Energy is given in units of $R_w=MG^2/\hbar^2$.

nel coupling creating these perturbations can be further characterized using the short-range scattering matrix $\underline{S}$, which is given by

$$\underline{S}=\frac{\underline{1}+i\underline{\widetilde{K}}}{\underline{1}-i\underline{\widetilde{K}}}, \tag{39}$$

where $\underline{1}$ is the identity matrix. The element $|S_{12}|^2$ is the probability that a particle in channel 2 could scatter into channel 1, in the course of a single collision for this value of J_z. Figure 7 shows that the channel coupling is small but nonzero. An energy diagram of the FEM solutions is provided in Fig. 8. The spectrum has an interesting qualitative feature in the Rydberg series overlap region. Each channel-2 state is followed by three channel-1 states and the pattern remains constant over the entire region. At energies where the states in the two channels are nearly degenerate, they mutually perturb each other, as can be seen in the Lu-Fano plot.

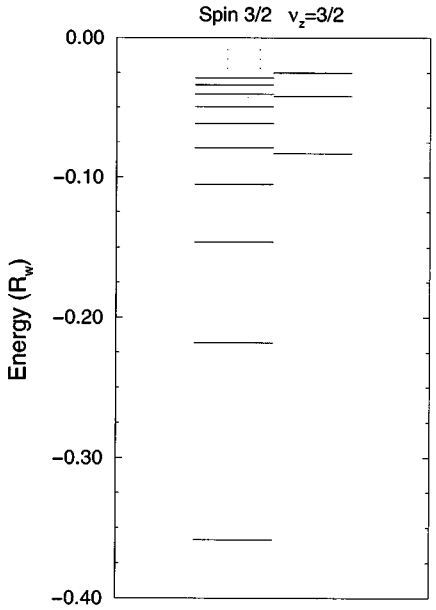

FIG. 8. Energy-level diagram for a spin-$\frac{3}{2}$ particle with $\nu_z=\frac{3}{2}$. The level diagram on the left indicates the bound state energies associated with channel 1. The interleaved channel 2 bound states are shown on the right. The ground and first excited states are not shown. Energies are given in units of $R_w=MG^2/\hbar^2$.

The possibility of experimentally measuring the multichannel spectrum can be investigated using the superconducting wire configuration proposed by Blümel and Dietrich [5]. They found that neutrons captured on a 45-nm-diameter superconducting wire should be detectable by rf absorption spectroscopy. We look into the feasibility of this type of experiment for a spin-2 particle trapped on a 0.1-μm-diameter superconducting wire. A rubidium ^{87}Rb atom was chosen for the calculations.

A practical experiment requires the particle to be kept away from the surface of the finite size wire to prevent absorption. Approximate formulas can be derived from the adiabatic potentials that relate the radial center of the ground-state wave function $\rho_{\max}$ and the half-width of the wave function δ to the particle's orbital angular momentum l and the current I passing through the wire. These equations read

$$\rho_{\max}=\frac{2\pi\hbar^2 l^2}{|\mu_B|\mu_0 MI} \tag{40}$$

and

$$\delta=\frac{2\pi\hbar^2(2l)^{3/2}}{|\mu_B|\mu_0 MI}. \tag{41}$$

These are used to find the lowest angular momentum state for a given current, which ensures the ground-state radial wave function resides outside the radius of the wire. Bound state energies for these states can then be calculated once the atomic magnetic moment $\vec{\mu}=(g_e\mu_B\vec{S}/\hbar)+(g_N\mu_N\vec{I}/\hbar)$ is known. Neglecting spin-spin interactions, an effective gyromagnetic ratio g_F for the atom can be calculated by coupling the nuclear $\vec{I}$ and electronic $\vec{S}$ spins and is given for the $F=2$ state by

$$g_2=\frac{1}{2}\left(1-4.1268\frac{m_e}{m_p}\right). \tag{42}$$

In this expression, m_e and m_p are the masses of the electron and proton, respectively. The magnetic moment for the atom is then given by

$$\vec{\mu}=\left(\frac{g_2\mu_B}{\hbar}\right)\vec{F}, \tag{43}$$

where $\vec{F}$ is now the total spin operator. The $F=2$ and $F=1$ manifolds are uncoupled, therefore we can neglect the $F=1$ states in our bound state energy calculations. Inserting the definition for the atomic magnetic moment [Eq. (43)] into the interaction potential [Eq. (1)] leads to the same form of the two-dimensional Schrödinger equation [Eq. (3)] as derived earlier. FEM bound state energies for a range of currents are provided in Table VII. The energy difference between the ground and first excited state ranges from 87 kHz to 12 MHz. rf probing of these states certainly seems feasible. The multichannel nature of the spectrum can be

TABLE VII. ^{87}Rb captured on a 50.0-nm radius superconducting wire. E_g is the ground state energy and ΔE represents the energy difference between the ground and first excited state. l is the lowest angular momentum state for which the ground-state wave function does not penetrate the wire.

I (mA)	l	E_g (Hz)	ΔE (Hz)
0.1	19	8.894×10^{5}	8.672×10^{4}
1.0	46	1.517×10^{7}	6.388×10^{5}
10.0	128	1.960×10^{8}	3.027×10^{6}
100.0	378	2.247×10^{9}	1.184×10^{7}

investigated for the 100-mA case using the adiabatic potentials (see Fig. 9). The angular momentum has been increased in order to move the centrifugal barrier outside the radius of the wire for all energies $E<0$. The first bound state associated with channel 2 has a binding energy of roughly 360 MHz, which is equivalent to the $n\sim476$ Rydberg state in channel 1. The energy splitting between the $n=476$ and $n=477$ states is approximately 750 kHz. Resolving the multichannel spectrum using a superconducting wire therefore seems a plausible, although obviously quite difficult, experiment.

VI. SUMMARY

We have investigated the bound state energy properties of neutral atoms with spin up to 2 that are trapped in the two-dimensional magnetic field associated with a straight line dc current. An adiabatic representation provides a simple qualitative picture of the quantum mechanical motion of the particle as well as a good approximation to the bound state energy levels. Two additional approaches for solving the coupled Schrödinger equations were presented. The direct FEM method provided excellent accuracy but proved to be quite memory intensive in the numerical computation for some cases. The combined FEM and R-matrix approach circumvented this problem with a small loss in accuracy. A two-channel QDT model was developed for a spin-$\frac{3}{2}$ particle. The model provides a way to calculate the strength of channel interactions that generate perturbations in the energy spectrum, and relate such strengths to interchannel scattering probabilities. Possibilities for experimental detection of the multichannel spectrum of a spin-2 particle were assessed. This analysis suggests that the spectrum could in principle be measured using a 0.1-μm superconducting wire.

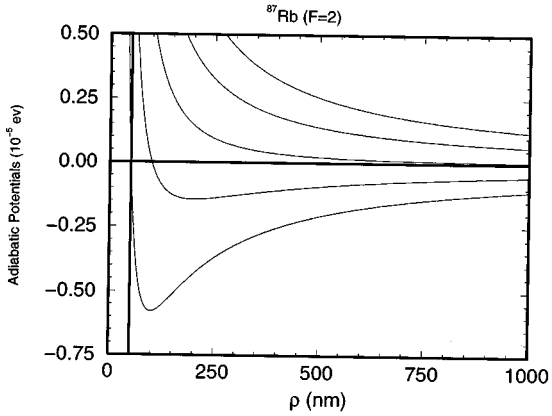

FIG. 9. Adiabatic potentials for ^{87}Rb in a $\nu_z = 493$ angular momentum state. A 100-mA current was used. The radius of the wire (50 nm) is also indicated on the graph.

ACKNOWLEDGMENTS

We thank John Bohn, William Clark, and Kurt Meyer for many enlightening discussions. This work was supported in part by the National Science Foundation.

[1] J. Schmiedmayer, Phys. Rev. A **52**, R13 (1995).
[2] J. Schmiedmayer, Appl. Phys. B **60**, 169 (1995).
[3] A. Lagendijk, I. F. Silvera, and B. J. Verhaar, Phys. Rev. B **33**, 626 (1986).
[4] G. P. Pron'ko and Yu. G. Stroganov, Sov. Phys. [Zh. Éksp. Teor. Fiz. **72**, 2048 (1977) JETP **45**, 1075 (1977)].
[5] R. Blümel and K. Dietrich, Phys. Rev. A **43**, 22 (1991).
[6] A. I. Voronin, Phys. Rev. A **43**, 29 (1991).
[7] L. V. Hau, J. A. Golovchenko, and M. M. Burns, Phys. Rev. Lett. **75**, 1426 (1995); K. Berg-Sørensen, M. M. Burns, J. A. Golovchenko, L. V. Hau, Phys. Rev. A **53**, 1653 (1996).
[8] J. Botero and J. Shertzer, Phys. Rev. A **46**, R1155 (1992).
[9] J. Shertzer and J. Botero, Phys. Rev. A **49**, 3673 (1994).
[10] M. Aymar, C. H. Greene, and E. Luc-Koenig (unpublished); U. Fano and A. R. P. Rau, *Atomic Collisions and Spectra* (Academic, New York, 1986); C. H. Greene, A. R. P. Rau, and U. Fano, Phys. Rev. A **26**, 2441 (1982).
[11] H. Friedrich, *Theoretical Atomic Physics* (Springer-Verlag, Berlin, 1990).
[12] M. J. Seaton, Rep. Prog. Phys. **46**, 167 (1983).
[13] H. Klar, Phys. Rev. A **15**, 1452 (1976).
[14] H. Klar and U. Fano, Phys. Rev. Lett **37**, 1132 (1976).
[15] K. J. Bathe, *Finite Element Procedures in Engineering Analysis* (Prentice Hall, Englewood Cliffs, NJ, 1976); K. J. Bathe and E. Wilson, *Numerical Methods in Finite Element Analysis* (Prentice Hall, Englewood Cliffs, NJ, 1976); L. R. Ram-Mohan, S. Saigal, D. Dossa, and J. Shertzer, Comput. Phys. **4**, 50 (1990).
[16] B. T. Smith *et al.*, *Matrix Eigensystem Routines - EISPACK Guide*. 2nd ed., Lecture Notes in Computer Science Vol. 6 (Springer-Verlag, New York, 1974).
[17] C. H. Greene, *Fundamental Processes of Atomic Dynamics* (Plenum, New York, 1988), p. 105; C. H. Greene and L. Kim, Phys. Rev. A **38**, 5953 (1988); H. Le Rouzo and G. Raseev, *ibid.* **29**, 1214 (1984).
[18] C. Greene and J. L. Dehmer (unpublished); C. H. Greene, Phys. Rev. A **20**, 656 (1979).